ELSEVIER

Journal of Power Sources 150 (2005) 192–201

POWER SOURCES

www.elsevier.com/locate/jpowsour

Nanocrystalline materials obtained by using a simple, rapid method for rechargeable lithium batteries

Alvaro Caballero [a], Manuel Cruz [a], Lourdes Hernán [a,*], Monserrat Melero [a], Julian Morales [a], Enrique Rodríguez Castellón [b]

[a] *Departamento de Química Inorgánica e Ingeniería Química, Campus de Rabanales, Edificio Marie Curie, Universidad de Córdoba, 14071 Córdoba, Spain*

[b] *Departamento de Química Inorgánica, Campus de Teatinos, Universidad de Málaga, Málaga, Spain*

Received 26 October 2004; received in revised form 10 February 2005; accepted 14 February 2005
Available online 31 March 2005

Abstract

Nanocrystalline oxides with either spinel (s.g. *Fd*3*m*) or layered (s.g. *R*3*m*) structures suitable as cathodic materials for lithium cells were prepared by using a simple, rapid method based on the thermal decomposition of mixed nanocrystalline oxalates formed by grinding hydrated salts and oxalic acid. Their structural and textural properties were determined by using X-ray photoelectron spectroscopy (XPS), X-ray diffraction (XRD), transmission electron microscopy (TEM), infrared spectroscopy (IR) and N_2 adsorption measurements. Well-crystallized spinels of formulae viz. $LiMn_2O_4$ and $LiNi_{0.5}Mn_{1.5}O_4$ with a thin sheet-like morphology and average particle size at ca. 30 nm were obtained by heating at temperatures as low as 400 °C for a short time. On the other hand, pure layered oxides ($LiCoO_2$ and $LiNi_{0.5}Co_{0.5}O_2$) required higher temperatures (800 °C), which resulted in greater particle sizes (average size ca. 100 nm). The electrochemical properties of these materials in lithium cells were studied from cyclic voltammetry and galvanostatic measurements. Cells made from the spinels exhibited good rate performance and the delivered capacities changed little over the charge–discharge rate range from *C*/4 to 4*C* (*C* is defined as the theoretical capacity delivered in 1 h). By contrast, the capacity values for the cells made from the layered oxides are strongly affected by the charge–discharge rates. Their increased particle size may be the origin of the poorer cell performance observed.

Keywords: Synthesis; Nanoparticles; Cathode materials; Lithium batteries

1. Introduction

The structures of materials commonly used to prepare positive electrodes for rechargeable lithium batteries generally consist of three- and two-dimensional frameworks capable of preserving the network upon insertion or extraction of lithium. Two paradigmatic compounds of these systems are $LiMn_2O_4$ and $LiCoO_2$, respectively, which have received much attention [1–4]. The operation of these batteries involves the diffusion of lithium ions within the bulk electrode particles, which governs their rate capability. Unfortunately, most appropriate electrode materials possess low chemical diffusion coefficients (below 10^{-9} cm^2 s^{-1}). The chemical coefficient of lithium, can be increased by tailoring open structures with the ability both to intercalate lithium reversibly and to deliver a high energy. An alternative way to compensate the effect of slow diffusion is by shortening the distance to be travelled by the lithium ions. The latter is the more attractive option and can be accomplished by reducing particle size. In this context, electrodes based on nanostructured materials have emerged as a valuable choice for improving battery performance, particularly as regards the ability of the electrode to withstand high discharge rates over an adequate cycle life [5,6].

One major hurdle at present is the difficulty of obtaining nanoparticles in precisely controlled size, composition and shape in an inexpensive, environmentally benign manner. In this respect, a number of synthetic routes have been used to prepare nanometric materials for lithium-ion battery

* Corresponding author. Fax: +34 957 218621.
E-mail address: iq1hepal@uco.es (L. Hernán).

0378-7753/$ – see front matter © 2005 Elsevier B.V. All rights reserved.
doi:10.1016/j.jpowsour.2005.02.013

electrodes based on sol–gel [7,8], coprecipitation [9], reduction [10], emulsion [11], hydrothermal [12,13], combustion [14,15], and mechanochemical [16,17] procedures. Most of these methods involve several steps and some are quite troublesome and expensive. In this work, we developed a simple, direct method for preparing nanometric materials with three- and two-dimensional structures for use as cathodes in lithium cells. The method relies on the synthesis of nanometric oxalates [18] prepared from highly hydrated salts ground in the presence of hydrated oxalic acid, which is followed by thermal decomposition of the precursors formed. The pyrolysis reaction preserves the nanometric size of the particles. Such a simple procedure allows highly homogeneous low–temperature lithium nanospinels, $LiNi_xMn_{2-x}O_4$ ($x = 0$; 0.5), to be prepared; by contrast obtaining nanoparticles of layered compounds such as $LiCoO_2$ and $LiNi_{0.5}Co_{0.5}O_2$ requires higher temperatures. The compounds obtained were characterized by using various analytical techniques including thermogravimetric analysis (TG), infrared spectroscopy (IR), electron microscopy (TEM and SEM), powder X-ray diffraction (XRD), photoelectron spectroscopy (XPS) and BET surface area measurements. The electrochemical activity of the nanoparticles as cathodes in lithium cells was tested with cyclic voltammetry and galvanostatic techniques.

2. Experimental

The procedure used to obtain nanometric Li-based oxides is based on one reported by Ye et al. [18] modified as follows: (i) excess oxalic acid was used to ensure complete conversion to mixed oxalates; (ii) further heating was applied to destroy the organic framework. The following compounds were thus obtained: $LiMn_2O_4$, $LiM_{0.5}Mn_{1.5}O_4$, $LiCoO_2$ and $LiCo_{0.5}Ni_{0.5}O_2$. The following precursors were used, in addition to $H_2C_2O_4{\cdot}2H_2O$, mixed in appropriate proportions, to obtain the corresponding oxides: $Li(ac){\cdot}1/3H_2O$, $Mn(ac)_2$ $4H_2O$, $Co(ac)_2{\cdot}4H_2O$ and $Ni(ac)_2$ $2H_2O$ (ac = acetate). All chemicals were supplied by Aldrich. The mixtures (ca. 5 g of mixed precursors and 2.5 g of $H_2C_2O_4{\cdot}2H_2O$) were ground in a planetary Restach ball mill at 60 rpm for 15 min, using agate balls and an agate jar. Then, 2 ml of ethanol was added to the slurry-like material formed and grinding continued for another 15 min. A strong smell of acetic acid was detected on opening the jar suggesting that grinding causes a metathesis reaction between the acetate salts and $H_2C_2O_4{\cdot}2H_2O$. The mixture was air-dried and stored in a dessicator for further characterization. Based on TG data, two different calcining temperatures were used for 1 h to prepare the compounds: 400 or 800 °C. Lithium contents were determined by atomic absorption spectroscopy, and Mn/Ni and Co/Ni ratios from energy-dispersive X-ray analysis (EDX) measurements. The average oxidation state of Mn was determined by conventional redox titration [19].

X-ray diffraction (XRD) patterns were recorded on a Siemens D5000 X-ray diffractometer using non-monochromated Cu Kα radiation and a graphite monochromator for the diffracted beam. The scanning conditions for structural refinement were 15–90° (2θ), a 0.03° step size and 12 s per step. Thermogravimetric measurements were made under ambient conditions, using a Cahn 2000 thermobalance at a heating rates of 10 °C min^{-1}. Transmission electron microscopy (TEM) images were obtained with a Phillips TEM operating at 100 keV and energy dispersive X-ray analyses (EDX) were performed with a JEOL 6400 scanning electron microscope. Specific surface areas were determined with a Micromeritic ASAP 2000 using N_2 gas as adsorbate. The pore size distribution was calculated by applying the Barret et al. [20] method to the desorption branch of the isotherms. FT-IR spectra were recorded over the range 4000–400 cm^{-1} on a Bomen MB-100 spectrometer. Each ground sample (0.5 mg) was mixed with 100 mg of spectroscopically pure dry KBr and pressed into disks before its spectrum was recorded. X-ray photoelectron spectra were obtained on a Physical Electronics PHI 5700 spectrometer using non–monochromatic Mg Kα radiation (300 W, 15 kV, 1253.6 eV) and a multi-channel detector. Spectra for the disc samples were recorded in the constant pass energy mode at 29.35 eV, using a 720 μm diameter analysis area. Binding energy (BE) values were referred to the C 1s peak (284.8 eV) from the adventitious contamination layer during data processing of the XPS spectra. The CA PHI ACCESS ESCA-V6.0 F software package was used for data acquisition and processing. A Shirley-type background was subtracted from all signals. Recorded spectra were always fitted using Gauss–Lorentz curves in order to more accurately determine the binding energy of the different element core levels. The error in BE was estimated to be ca. ±0.1 eV.

Electrochemical measurements were made on CR2032 coin-type cells supplied by Hohsen. The cathode was prepared by pressing, in a stainless steel grid, ca. 10 mg of active Lithium metal (supplied by Strem) was used as anode and isolated from the cathode by means of a porous propylene film. The electrolyte, supplied by Merck, was 1 M anhydrous $LiPF_6$ in a 1:1 mixture of ethylene carbonate and dimethyl carbonate. Cells were assembled in an M-Braun glove-box. Cyclic voltammetry was performed with a Solartron 1286 Electrochemical Interface controlled via the CorrWare software package as run on a PC Pentium II computer. Curves were recorded at a scan rate of 50 μV s^{-1}. Charge–discharge cycles were performed on a McPile II (Biologic) potentiostat–galvanostat system under a galvanostatic regime. All measurements were made at least in duplicate in order to check the reliability of the electrochemical tests.

3. Results and discussion

3.1. Synthesis, textural and structural properties of the materials

Fig. 1 shows the TG curves obtained over the temperature range 25–800 °C for the different precursors. The weight loss

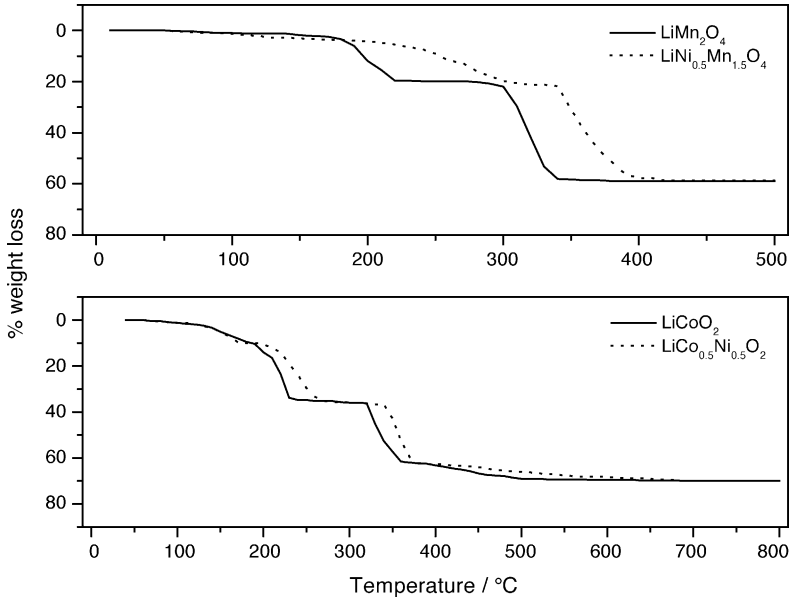

Fig. 1. TG curves for the ground precursors.

for the spinel precursors occurred below 400 °C and in two steps, consistent with water release and pyrolysis of the organic framework. The presence of Ni increased the precursor decomposition temperature. Above 400 °C, the layered oxide precursors exhibited a third step reflecting a slow weight loss that extended beyond 700 °C. The presence of Ni also increased the temperature of the weight loss steps slightly. Based on the TG data, we initially used a calcining temperature of 400 °C to prepare the different compounds. The low-temperature synthesis was carried out in two steps: heating at 25 °C min^{-1} to 400 °C, and holding for 1 h. Fig. 2 shows selected XRD patterns. All lines for the Mn-containing samples except the weak one at 26.66° (2θ) assigned to SiO_2 impurities introduced during grinding, were indexed in a spinel structure (s.g. *Fd*3*m*) (Fig. 2a and b); on the other hand, the XRD patterns for the Co-containing samples were more complex and included various peaks that could not be assigned to a layered structure (s.g. *R*3*m*). Most such peaks corresponded to unreacted CoO and NiO (Fig. 2c). In order to increase sample purity, the calcining temperature was raised to 800 °C, using the same heating conditions as in the low-temperature synthesis. The short heating time used was intended to avoid syntering and the subsequent increased particle size. Essentially, the main difference was narrowing of the peaks; however impurities such as NiO persisted. This entailed using a slight lithium excess (ca. 10%) to offset the potential loss of Li_2O by volatilization and promote Li site ordering. The use of a Li excess is quite common in preparing of $LiCo_{1-y}Ni_yO_2$ compounds [21]. Layered phases were invariably obtained under these conditions.

IR spectroscopy is an effective choice for detecting impurities such as undecomposed organic components of the precursors in this context. Fig. 3 shows several selected IR spectra. The spinels exhibited no bands at ca. 3000 cm^{-1}, which are assigned to ν(C–H), or at 1500–1550 cm^{-1}, which are assigned to ν(C=O) coupled with ν(C–C); this excluded the presence of traces of initial acetate and/or oxalate complexes in the calcined samples. The spectra also confirmed the absence of carbonate groups, which excluded the formation of Li_2CO_3 in the low-temperature spinels. However, they exhibited a band at ca. 1090 cm^{-1} assigned to the stretching mode of the Si–O bond [22], which confirmed the presence of silica impurities coming from the mill balls and jar. Such impurities were also detected by XRD and XPS, but in contents less than 4%. This band was barely detected for the layered oxides; their spectra, however, exhibited weak signals at ca. 1500 cm^{-1} and below 1000 cm^{-1}, two regions where the stretching bands of CO_3^{2-} ion appear. Preliminary XPS spectra also exhibited a signal at 289.7 eV for the C 1s photoemission peak, assigned to this ion, the content in which was estimated to be ca. 3%. Therefore, part of the Li excess is combined as Li_2CO_3. The water solubility of this salt was used to remove it from the calcined layered oxides by washing. Its removal was further confirmed by the IR and XPS spectra.

The results of the chemical analysis are shown in Table 1. The Mn/Ni ratio for the spinel phase obtained from the EDX data was somewhat higher than the stoichiometric value of 3. Also, the XPS data revealed the presence of an Mn excess at surface level that was somewhat greater than that calculated from the EDX measurements. The EDX results for the layered phases were quite consistent with the expected stoichiometry. The average oxidation state (Z) obtained for the Ni spinel was slightly smaller than 4; this suggests the presence of Mn^{3+}, further confirmed by the electrochemical determinations, as shown below.

Fig. 4 shows selected TEM images for some samples. As can be seen, the spinel particles adopted a thin sheet-like mor-

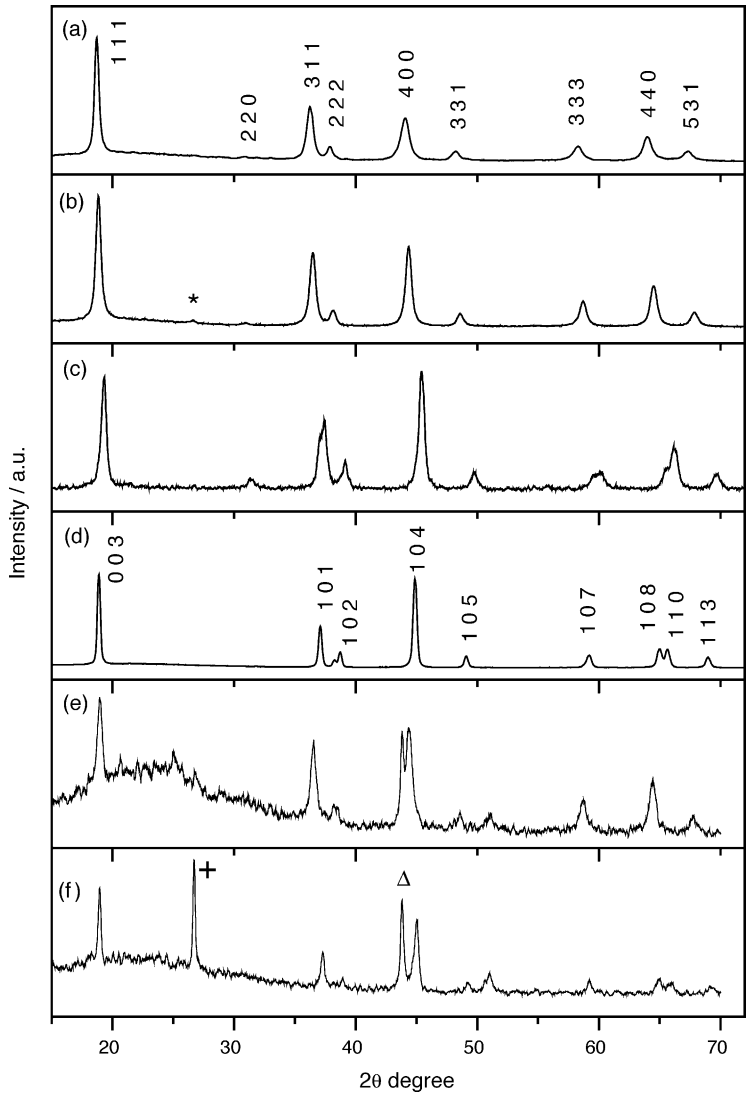

Fig. 2. X-ray diffraction patterns for (a) $LiMn_2O_4$, (b) $LiNi_{0.5}Mn_{1.5}O_4$ and (c) $LiCoO_2$, all heated at 400 °C, and (d) $LiCo_{0.5}Ni_{0.5}O_2$ heated at 800 °C and washed with diluted HCl acid; (e) and (f) samples (b) and (d), respectively, after one hundred of cycles ((*) silica, (+) graphite, (Δ) stainless steel).

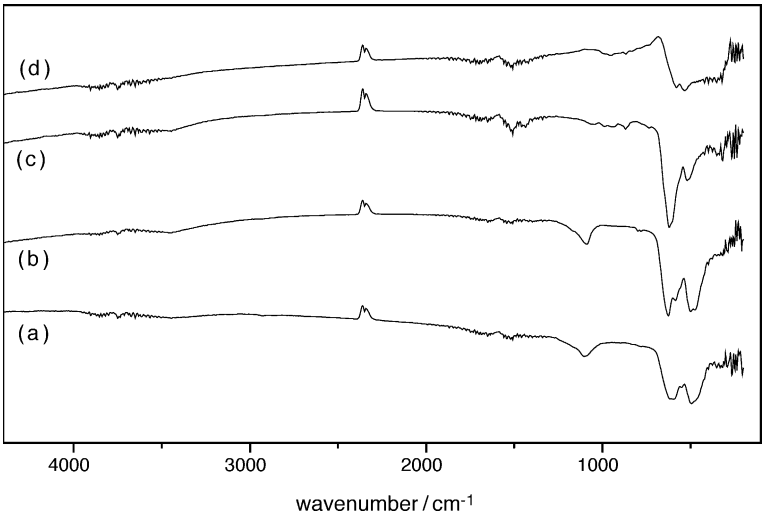

Fig. 3. FT-IR spectra for (a) $LiMn_2O_4$, (b) $LiNi_{0.5}Mn_{1.5}O_4$, (c) $LiCoO_2$ and (d) $LiCo_{0.5}Ni_{0.5}O_2$.

Table 1
Compositional values and textural properties of nanocrystalline oxides

Sample	T	Mn^{n+}	Mn/Ni, Co/Ni[a]	Li/M	Nominal formula	S_{BET} ($m^2\ g^{-1}$)	Pore size	Crystallite size[b]
$LiMn_2O_4$	400	3.52	–	0.49	$Li_{0.98}Mn_{1.99}O_4$	46.8	20.3	38
$LiNi_{0.5}Mn_{1.5}O_4$	400	3.89	3.20	0.47	$Li_{0.99}Ni_{0.48}Mn_{1.55}O_4$	60.1	17.1	26
$LiCoO_2$	800	–	–	0.98	$Li_{0.99}Co_{1.01}O_2$	13.3	–	90
$LiNi_{0.5}Co_{0.5}O_2$	800	–	1.02	0.99	$Li_{0.98}Ni_{0.49}Co_{0.50}O_2$	2.0	–	120

[a] EDX measurements.
[b] X-ray crystallite size (nm).

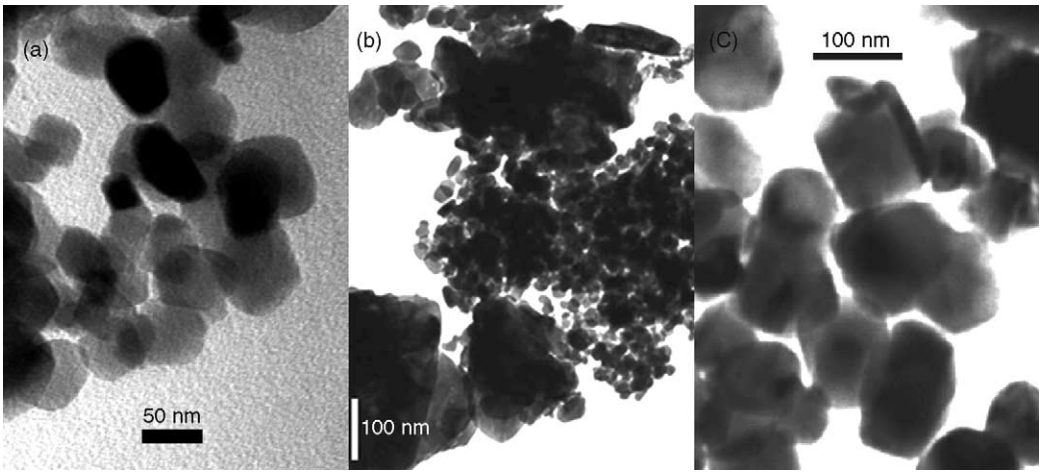

Fig. 4. Transmission electron micrographs for (a) $LiNi_{0.5}Mn_{1.5}O_4$ obtained at 400 °C, (b) $LiMn_2O_4$ obtained at 400 °C in the absence of oxalic acid and (c) $LiNi_{0.5}Co_{0.5}O_2$ obtained at 800 °C.

phology and were less than 40 nm in size. Crystallite sizes, which were independent of the crystal direction consistent with the three-dimensional network of the spinel, were close to those calculated from the TEM images. Therefore, the particles consist of a single coherent diffracting domain. The nitrogen adsorption isotherms, Fig. 5a, show a hysteresis loop, the shape of which corresponds with the H3 in the Boer classification [23]. Specific surface areas and average pore sizes are listed in Table 1. Taking into account the smooth particle surfaces observed, the origin of the mesoporous system must be

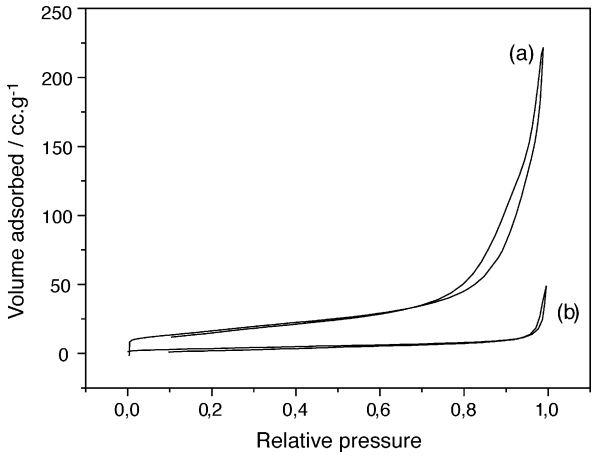

Fig. 5. N_2 adsorption/desorption isotherms for (a) $LiNi_{0.5}Mn_{1.5}O_4$; (b) $LiNi_{0.5}Co_{0.5}O_2$.

the voids between individual particles forming clusters (see Fig. 4a). In fact, the H3 type is ascribed to slit-shaped porous generated by particle aggregates. Similar textural properties have recently been reported for $LiNi_xMn_{2-x}O_4$ nanoparticles prepared by a combustion method [12]. The role played by oxalic acid dihydrate as a reaction medium is illustrated in the image of Fig. 4b, which includes the $LiMn_2O_4$ spinel formed by calcining the ground acetate precursors in the absence of the acid. A wider particle size distribution was observed and nanoparticles coexisted with microparticles. The formation of nanometric mixed oxalates on grinding therefore seems to be a necessary prior step in the synthesis of these nanometric materials. Also, the hydration water has been pinpointed as the medium enhancing nucleation and growth of the reaction products [18]. However, hydration water in the acetates by itself does not ensure a uniform nanometric size distribution.

As stated above, obtaining single phases of the layered oxides required using higher calcination temperatures (800 °C). This introduced significant differences in textural properties from the spinel phases (see Fig. 4c and Table 1). Thus, particles were larger (most exceeded 100 nm in size) and the nitrogen adsorption isotherm were of type II in the BDDT classification, Fig. 5b, which corresponds to non-porous or macroporous solid; also, the specific surface area was lower, particularly for the $LiCo_{0.5}Ni_{0.5}O_2$ oxide. In spite of the layered structure, crystallite size was also independent of the crystallographic direction and the average value obtained from the three strongest reflections was similar to that cal-

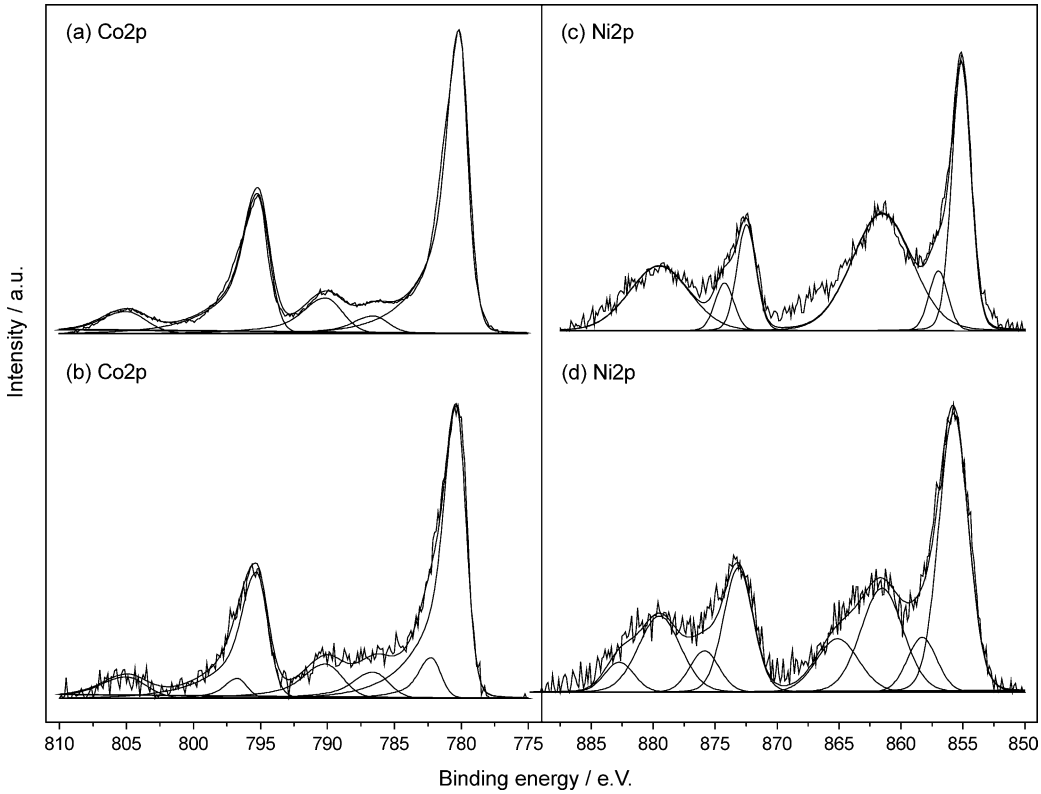

Fig. 6. X-ray photoelectron spectra for the (a) Co 2p ($LiCoO_2$); (b) Co 2p ($LiCo_{0.5}Ni_{0.5}O_2$); (c) Ni 2p ($LiNi_{0.5}Mn_{1.5}O_4$); (d) Ni 2p ($LiCo_{0.5}Ni_{0.5}O_2$) regions.

culated from the TEM images. The particle morphology of $LiCo_{0.5}Ni_{0.5}O_2$ was similar to that of $LiCoO_2$; however, the particle size of the former was somewhat greater, consistent with the BET surface area and crystallite size (Table 1).

The electronic structure was studied from the XPS spectra of Fig. 6. The BE values for Mn hardly changed with the substituting element; also, that for the Mn $2p_{3/2}$ peak, 642.4 eV, was somewhat higher than those reported for $NiMn_2O_4$ (formally with Mn^{3+} as the main component) [24] and $LiM_{0.2}Mn_{1.8}O_4$ (M = Fe, Co, Ni) [19]. This must be related to the increased content in Mn^{4+} of the spinels as calculated from the average oxidation states. Moreover, the absence of the satellite peak clearly observed 5 eV above the $2p_{3/2}$ component [25] for Mn^{2+} rules out the presence of manganese in this oxidation state. Unfortunately, the electronic differences between the two spinels are too subtle to be detected in the Mn 2p spectra.

The Co 2p spectra for the two layered oxides are shown in Fig. 6a and b. The spectral profiles differ only slightly: the Co $2p_{3/2}$, $2p_{1/2}$ peaks for the $LiCoO_2$ compound are somewhat less asymmetric. This allowed the peaks to be fitted to a single component. The binding energies for Co $2p_{3/2}$, 780.2 eV, was close to those reported for $LiCoO_2$ (779.8 eV) [26] and CoOOH (780.0 eV), and also similar to that for CoO [24]. However, the satellite peak clearly observed at 790.0 eV and the $2p_{3/2}$–$2p_{1/2}$ doublet separation (15.04 eV) were typical of Co^{3+}. The greater asymmetry of the Co $2p_{3/2}$ peak for $LiCo_{0.5}Ni_{0.5}O_2$ was consistent with two components at 780.4 and 782.3 eV. The former, which was the stronger, was assigned to Co^{3+}, in a similar environment to that for $LiCoO_2$. This is consistent with the results of recent electronic structure studies carried out by X-ray absorption fine structure (XAFS) [27] and X-ray absorption (XAS) spectroscopies [28]. The assignation of latter, weaker component is controversial; an interaction of Co with Ni through bridge oxygens is one origin plausible. On the other hand, the shape and intensity of the satellites are scarcely affected by the presence of Ni.

The Ni 2p spectra for the spinel and layered oxide are shown in Fig. 6c and d. They exhibit differences that warrant some comment. First, the “shake up” satellites, which are strongly dependent on the particular chemical state, can be fitted to a variable number of components (one for the spinel and two for the layered oxide). Second, although the shape of the Ni $2p_{3/2}$ and $2p_{1/2}$ profiles is rather similar, in both samples they can be fitted to two components, the difference in BE between which is significant. Thus, the Ni $2p_{3/2}$ main component for the spinel is at 855.1 eV and can be ascribed to Ni^{2+} ions at octahedral sites in the spinel structure. This value is consistent with those reported for other Ni and Mn spinels (e.g., 855.2 eV for $NiMn_2O_4$) [24]. The equivalent peak for $LiCo_{0.5}Ni_{0.5}O_2$ appears at 855.8 eV, i.e., 0.7 eV above the principal line for the spinel. This difference and the disparate satellite structure are inconsistent with Ni^{2+} as the main oxidation for the layered compound, as found by Montoro et al. from XAS spectra [28]. Our data are better

Table 2
Refinement conditions for the X-ray data

Fraction	Spinel		Layered oxide	
	Atom	$x=y=z$[a]	Atom	x, y, z[a]
Variable	Li[b]	1/8	Li[b]	0, 0, 0
Variable	Mn[b]	1/8	Ni[b]	0, 0, 0
Fixed	Mn[c]	1/2	Co[c]	0, 0, 0.5
Fixed	Li[c]	1/2	Li[c]	0, 0, 0.5
Fixed	Ni[c]	1/2	Ni[c]	0, 0, 0.5
1	O	x[d]	O	0, 0, z[d]

[a] Coordinates.
[b] For total occupancy of 8*a* and 3*a* by both ions for the spinel and layered oxide, respectively.
[c] Values imposed by the stoichiometry.
[d] The coordinate is approximately 0.254–0.257 and 0.241–0.244 for the spinels and layered oxides, respectively, depending on the sample composition.

interpreted by assuming Ni^{3+} to be the main oxidation state, consistent with the electronic structure determined by XAFS analysis [27]. For the two spectra, the fitting provides a second weaker peak on the left-hand side of the main component the origin of which is uncertain. We wonder whether such a component may be a mathematical artefact resulting from the deconvolution of the profile and a consequence of the "shake-up" satellite overlapping with the 2p emission peak. Theoretical calculations beyond the scope of this work are required to ascertain the true meaning of this component.

The structural characterization of the different compounds was completed by subjecting the XRD data to Rietveld refinement [29] using the GSAS software suite [30]. The spinels and layered oxides were refined in the *Fd*3*m* and *R*3*m*, respectively, using the conditions shown in Table 2. The results thus obtained are given in Table 3. Both spinels were found to be essentially stoichiometric and their compositions consistent with those obtained by chemical analysis (Table 1); this confirm the presence of excess Mn relative to the nominal formula $LiNi_{0.5}Mn_{1.5}O_4$. The appearance of the (2 2 0) reflection as a weak peak confirms that 8*a* sites are occupied by a small fraction of the transition elements. Based on the crystal field model, Ni^{2+} ions have a strong tendency to occupy octahedral positions (16*d*); therefore Mn was forced to occupy tetrahedral positions (8*a*). The cell parameters for the layered compounds increased upon substitution of Co^{3+} by Ni^{3+}, consistent with the larger ionic radius of the latter cation ($r_{Co^{3+}} = 0.54$ Å; $r_{Ni^{3+}} = 0.56$ Å, in a low-spin configuration) [31]; however, the *c*/3*a* ratio was somewhat smaller (1.655 for $LiNi_{0.5}Co_{0.5}O_2$ and 1.664 for $LiCoO_2$). The higher such a ratio is, the smaller is the transition metal content in the lithium layer [32]. The value for $LiCoO_2$ is highly consistent with that reported for this compound; the best fit was obtained with complete occupancy of 3*a* and 3*b* sites by Li and Co, respectively. The smaller value for the Ni–Co system is consistent with the XR refinement as the best fit was obtained for a small fraction of transition element in the lithium layer (see Table 3).

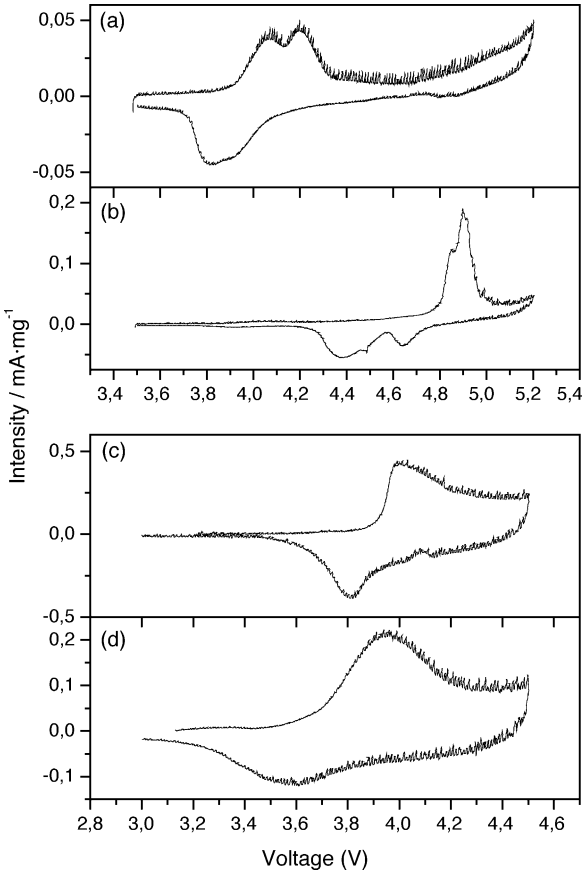

Fig. 7. Cyclic voltammograms for (a) $LiMn_2O_4$; (b) $LiNi_{0.5}Mn_{1.5}O_4$; (c) $LiCoO_2$; (d) $LiCo_{0.5}Ni_{0.5}O_2$.

3.2. Electrochemical properties

Fig. 7 shows the cyclic voltammograms (CVs) for the four studied samples. The anodic scans for the spinels exhibit two regions of electrochemical activity over the ranges 3.9–4.4 and 4.6–5.2 V. The former is related to the Mn^{3+}/Mn^{4+} redox couple. The two-step process reflects in the two redox peaks, which result from splitting of the original Li positions in 8*a* [33]. The electrochemical response of the Ni spinels in

Table 3
Cation distribution, lattice parameters and *R* factors for the different samples calculated from XRD data

Sample	Composition	a, c (Å)	R_{wp}	R_p
$LiMn_2O_4$	$[Li_{0.92}Mn_{0.08}]_{8a}[Li_{0.08}Mn_{1.92}]_{16d}O_4$	8.2344(5)	11.7	8.7
$LiNi_{0.5}Mn_{1.5}O_4$	$[Li_{0.937}Mn_{0.063}]_{8a}[Li_{0.12}Ni_{0.44}Mn_{1.44}]_{16d}O_4$	8.1815(6)	11.4	8.2
$LiCoO_2$	$[Li]_{3a}[Co]_{3b}O_2$	2.8164(6), 14.0595(3)	12.5	8.9
$LiCo_{0.5}Ni_{0.5}O_2$	$[Li_{0.94}Ni_{0.06}]_{3a}[Li_{0.06}Ni_{0.44}Co_{0.5}]_{3b}O_2$	2.8472(7), 14.1379(6)	11.2	8.4

the 3.9–4.3 V region is barely detected, consistent with the high oxidation state of Mn in the spinel and the consequently small fraction of Mn^{3+} present (see Table 1). The main electrochemical activity develops in the 4.7–5.0 V region, where a double peak appears associated to the $Ni^{2+} \rightarrow Ni^{4+}$ process, the mechanism of which reportedly involves two cubic/cubic two-phase reactions [34]. This process is reversible and takes place at a somewhat lower voltage. The cyclic voltamogramm for $LiCoO_2$ is similar to that previously reported for this compound and the asymmetry of the peaks is related to order/disorder phase transitions [35]. The anodic peak for de-intercalation of Li^+ in $LiNi_{0.5}Co_{0.5}O_2$ is more symmetric and appears at 3.95 V; it is somewhat smaller than that for $LiCoO_2$ and occurs over a broad potential range. The reduction peak is also rather symmetric and broad, and is centred at 3.6 V.

The electrochemical properties were also tested galvanostatically over the ranges 3.5–4.5 V ($LiMn_2O_4$), 3.5–5.0 V ($LiNi_{0.5}Mn_{1.5}O_4$) and 2.0–4.5 V (layered oxides) at different rates. The variation of the discharge capacity for the four compounds at the lower rate tested (*C*/4) is shown in Fig. 8a and b. The cycling properties of the spinels, Fig. 8a, were found to be quite similar and their capacities to slowly fade with cycling,

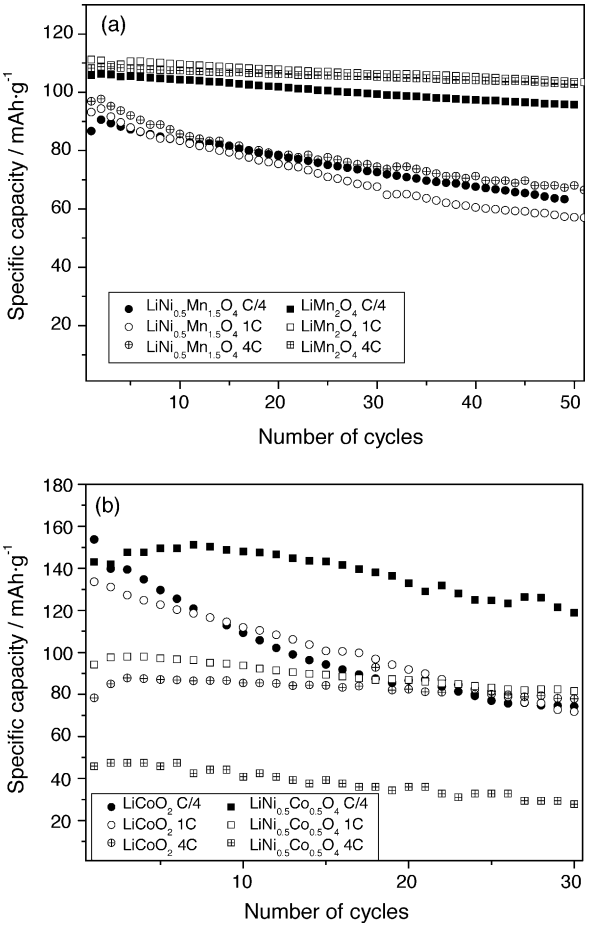

Fig. 8. Influence of the charge–discharge rate on the discharge capacity of Li/Li–Ni–Mn(Co)–O cells obtained from (a) spinels and (b) layered oxides.

the drop being somewhat more marked for the Ni spinel. Moreover, the average capacity delivered by this spinel in the first few cycles was below 90 mAh g^{-1} and thus far from the theoretical capacity of 148 mAh g^{-1}. Values as low as those found in this work have been reported for nanocrystalline $LiNi_{0.5}Mn_{1.5}O_4$, prepared at 700 °C [36]. The suggestion of Manthiram and Kim [37] that high calcination temperatures usually result in improved electrode performance through decreased particle surface roughness and improved crystalline, is applicable to this system. The first discharge values for $LiCo_{0.5}Ni_{0.5}O_2$ and $LiCoO_2$ electrodes at *C*/4 rate were quite similar (about 135–140 mAh g^{-1}), Fig. 8b. However, their cycling properties differed considerably. Thus, the capacity of the $LiCo_{0.5}Ni_{0.5}O_2$ electrode, after the first fifteen cycles, faded slowly with cycling (capacity loss per cycle was ca. 0.7%); on the other hand, the capacity of the $LiCoO_2$ electrode faded faster (to only 83 mAh g^{-1}, which is less than 40% of the initial value, after the twentieth cycle). The cyclic voltammograms can provide an explanation for the poorer electrochemical properties of $LiCoO_2$. Thus, the oxidation and reduction processes of $LiCo_{0.5}Ni_{0.5}$ O_2 only exhibit one major peak, centred at 3.94 and 3.60 V, respectively. On the other hand, the peaks for $LiCoO_2$ are more asymmetric and consist of at least two components, which suggests the occurrence of multi-phase reactions during the lithium extraction/insertion process. This involves major structural changes that result in more pronounced degradation of the electrode performance.

One of the advantages of nanometric materials in lithium cells is the high rate performance they possess by virtue of their short diffusion paths for lithium ions, as fully confirmed for the spinels in Fig. 8a. The delivered capacity and the cycling properties undergo little changes with the charge–discharge rates, with a slight tendency to increase as the rate increases. The best performance was shown by the cell made from $LiMn_2O_4$, the capacity loss of which is about 0.1% per cycle, independently of the charge–discharge rate. For the Ni–Mn spinel, the variation of the capacity with cycling is more irregular and the capacity loss is somewhat more affected by the rate, 15, 24 and 20 % for *C*/4, 1*C* and 4*C*, respectively, at the 30 cycle. In contrast, the cell made from $LiCo_{0.5}Ni_{0.5}O_2$ is significantly affected by the charge–discharge rate, as shown in Fig. 8b. The capacity significantly decreases with increasing the charge–discharge rate, from 144 to 44 mAh g^{-1}, for *C*/4 and 4*C* rate, respectively. Moreover, the capacity fading with cycling increases with the charge–discharge (capacity loss at the 30 cycle 13, 18 and 31% for *C*/4, 1*C* and 4*C* rate, respectively). The electrochemical behaviour of $LiCoO_2$ is intermediate between that of $LiCo_{0.5}Ni_{0.5}O_2$ and $LiNi_{0.5}Mn_{1.5}O_4$. At *C*/4 and 1*C* rates, the cycling properties are similar and resemble to those observed for $LiNi_{0.5}Mn_{1.5}O_4$. At 4*C*, the discharge capacity undergoes an appreciable decrease, like to that found for $LiCo_{0.5}Ni_{0.5}O_2$, but the capacity retention improves, probably related with the smaller amount of lithium extruded from the structure.

Differences in structural changes undergone by the oxides on cycling can be discarded as the origin of the distinct electrochemical behaviour observed. All compounds maintained the basic framework of the original structure upon extensively cycling, as revealed the XRD patterns included in Fig. 2e and f. Although the peak intensity become smaller, compared to the pristine samples, the main reflections are still present. In contrast, a fair correlation exists between particle size and the electrochemical response of the compounds. Thus, the cells made from the spinels that possess the smaller particle size, yield the best electrochemical response. The better performance of $LiMn_2O_4$ compared with $LiNi_{0.5}Mn_{1.5}O_4$, can be ascribed to the different voltage window for recording the charge–discharge curves. The upper voltage of 5.0 V used for the Ni–Mn spinel could affect either to the electrolyte stability [38] or the oxygen packing with the release of oxygen [39]. This should result in a greater damage of the cell components, thus leading to a more pronounced fade of the discharge capacity with cycling. The greatest influence exerted by the rate on the discharge capacity is observed for the $LiCo_{0.5}Ni_{0.5}O_2$ sample that has also the greatest size, thus increasing the diffusion paths for Li ions. The intermediate electrochemical response of the $LiCoO_2$ sample, compared with the spinels and the $LiCo_{0.5}Ni_{0.5}O_2$ sample, is also consistent with its particle size, smaller than that of the Co–Ni sample but greater than those of the spinels. Various modifications on the synthesis method for obtaining these oxides in particle sizes within the range of the spinels are currently being tested with a view to improving their rate capabilities.

4. Conclusions

Well-crystallized nanometric lithium spinels of homogeneous size of ca. 30 nm were synthesized at 400 °C by a simple method that makes use of nanocrystalline mixed oxalates prepared by a solid state reaction at ambient temperature with the help of a grinding procedure. These spinels were tested in lithium cells and showed good performance at charge–discharge rates as high as 4*C*. The method is also suitable for the synthesis of lithium layered oxides, but the preparation of well-crystallized compounds requires to attain to higher temperatures, ca. 800 °C. Under these conditions, particle size notably increased (average particle size about 100 nm). This increase is prejudicial to the cell rate capability. Thus, the delivered capacity by the $LiCo_{0.5}Ni_{0.5}O_2$ sample, that with the greatest particle size, significantly decreased on increasing the charge–discharge rate.

Acknowledgements

This work was supported by Junta de Andalucía (Group FQM-175) and Ministerio de Ciencia y Tecnología (Project MAT2002-04477-C02-02).

References

[1] M.M. Thackeray, W.I.F. David, P.G. Bruce, J.B. Goodenough, Mater. Res. Bull. 18 (1983) 461.
[2] J.M. Tarascon, E. Wang, F. Shokoohi, W.R. MacKinnon, S. Coulson, J. Electrochem. Soc. 137 (1991) 2864.
[3] K. Mizushima, P.C. Jones, P.J. Wiseman, J.B. Goodenough, Mater. Res. Bull. 15 (1980) 783.
[4] T. Nagaura, K. Tazawa, Prog. Batteries Sol. Cells 9 (1990) 20.
[5] C.R. Slides, N. Li, C.J. Patrissi, B. Scrosati, C.R. Martin, MRS Bull. (2002) 604.
[6] A. Singhal, G. Skandan, G. Amatucci, F. Badway, N. Ye, A. Manthiram, H. Ye, J.J. Xu, J. Power Sources 129 (2004) 38.
[7] X.N. Wang, X.Y. Chen, L.H. Gao, M.Ji. Zheng, T. Shen, Z. Zhang, J. Cryst. Growth 256 (2003) 123.
[8] C.J. Curtis, J. Wang, D.L. Schulz, J. Electrochem. Soc. 151 (2004) 590.
[9] N. Treuil, C. Labrugère, M. Menetrier, J. Portier, G. Campet, A. Deshayes, J.-C. Frison, S.-J. Hwang, S.-W. Song, J.-H. Choy, J. Phys. Chem. B 103 (1999) 2100.
[10] D. Im, A. Manthiram, J. Electrochem. Soc. 149 (2002) A1001.
[11] C.H. Lu, H.C. Wang, J. Mater. Chem. 13 (2003) 428.
[12] Y.C. Zhang, H. Wang, B. Wang, Mater. Res. Bull. 37 (2002) 1411.
[13] Z. Liu, A.-L. Wang, X. Liu, M. Wu, D. Li, Z. Zeng, J. Solid State Chem. 177 (2004) 1585.
[14] M.G. Lazarraga, L. Pacual, H. Gadjov, D. Kovacheva, K. Petrov, J.M. Amarilla, R.M. Rojas, M.A. Martín-Luengo, J.M. Rojo, J. Mater. Chem. 14 (2004) 1640.
[15] Y.-S. Hong, Y.J. Park, K.S. Ryu, S.H. Chang, M.G. Kim, J. Mater. Chem. 14 (2004) 1424.
[16] H.J. Choi, K.M. Lee, G.H. Kim, J. Am. Ceram. Soc. 84 (2001) 242.
[17] S.H. Kang, J.B. Goodenough, L.K. Rabenberg, Electrochem. Solid State Lett. 4 (2001) A49.
[18] X.R. Ye, D.Z. Jia, J.Q. Yu, X.Q. Xin, Z. Xue, Adv. Mater. 11 (1999) 941.
[19] L. Hernán, J. Morales, L. Sánchez, E. Rodríguez Castellón, M.A.G. Aranda, J. Mater. Chem. 12 (2002) 734.
[20] E.P. Barret, L.G. Joyner, P.P. Halenda, J. Am. Chem. Soc. 73 (1951) 373.
[21] R.K.B. Gover, R. Kanno, B.J. Mitchell, M. Yonemura, Y. Kawamoto, J. Electrochem. Soc. 147 (2000) 4045.
[22] J.A. Navio, M. Macías, G. Colón, P.J. Sánchez Soto, L. Augugliaro, Appl. Surf. Sci. 81 (1994) 325.
[23] J.H. de Boer, in: D.H. Everett, S. Stone (Eds.), Structure and Properties of Porous Materials, Butterworths, London, 1958.
[24] J.F. Moulder, W.F. Stickle, P.E. Sool, K.D. Bomber, Handbook of X-ray Photoelectron Spectroscopy, Perkin-Elmer, Eden Prairie, 1992.
[25] A.E. Bocquet, T. Mizokawa, T. Saitoh, H. Namatame, A. Fujimori, Phys. Rev. B 46 (1992) 3777.
[26] J.C. Dupin, D. Ganbeau, I. Martin-Litas, P. Vinatier, A. Levasseur, J. Electron. Espectrosc. Rel. Phenom. 120 (2001) 55.
[27] I. Nakai, T. Nakagome, Electrochem. Solid State Lett. 1 (1998) 259.
[28] L.A. Montoro, M. Abate, J.M. Rosolen, J. Electrochem. Soc. 147 (2000) 1651.
[29] H.M. Rietveld, J. Appl. Crystallogr. 2 (1969) 65.
[30] A.C. Larson, R.B. Von Dreele, Los Alamos National Lab. Rep. No. LA-UR-86-748, 1994.
[31] R.D. Shannon, Acta Crystallogr. A32 (1976) 751.
[32] J.K. Ngala, N.A. Chernova, M. Ma, M. Mamak, P.Y. Zavalij, M.S. Whittingham, J. Mater. Chem. 14 (2004) 214.
[33] A. Ott, P. Endres, V. Klein, B. Fuchs, A. Jager, H.A. Mayer, S.K. Sack, H.W. Paas, K. Brandt, G. Filoti, V. Kunczer, M. Rosenberk, J. Power Sources 72 (1998) 1.
[34] K. Ariyoshi, Y. Iwakoshi, N. Nakayama, T. Ohzuku, J. Electrochem. Soc. 151 (2004) 296.

[35] M. Antaya, K. Cearns, J.S. Preston, J.N. Reimers, J.R. Dahn, J. Appl. Phys. 76 (1996) 2799.
[36] S.T. Myung, S. Komaba, N. Kumagai, H. Yashiro, H.T. Chung, T.H. Cho, Electrochim. Acta 47 (2002) 2543.
[37] A. Manthiram, J. Kim, Chem. Mater. 10 (1998) 2895.
[38] P. Arora, R.E. White, M. Doyle, J. Electrochem. Soc. 145 (1998) 3647.
[39] A. Caballero, L. Hernán, M. Melero, J. Morales, M. Angulo, J. Electrochem. Soc. 151 (2005) A6.